Wind and Structures, Vol. 10, No. 5 (2007) 437-462
DOI: http://dx.doi.org/10.12989/was.2007.10.5.437

Impinging jet simulation of stationary downburst flow over topography

M.S. Mason†

School of Civil Engineering, University of Sydney, Sydney, NSW 2006, Australia

G.S. Wood

Cermak Peterka Petersen, Pty. Ltd., St. Peters, NSW 2044, Australia

D.F. Fletcher

School of Chemical and Biomolecular Engineering, University of Sydney, Sydney, NSW 2006, Australia
(Received May 15, 2007, Accepted September 3, 2007)

Abstract. A non-translating, long duration thunderstorm downburst has been simulated experimentally and numerically by modelling a spatially stationary steady flow impinging air jet. Velocity profiles were shown to compare well with an upper-bound of velocity measurements reported for full-scale microbursts. Velocity speed-up over a range of topographic features in simulated downburst flow was also tested with comparisons made to previous work in a similar flow, and also boundary layer wind tunnel experiments. It was found that the amplification measured above the crest of topographic features in simulated downburst flow was up to 35% less than that observed in boundary layer flow for all shapes tested. From the computational standpoint we conclude that the Shear Stress Transport (*SST*) model performs the best from amongst a range of eddy-viscosity and second moment closures tested for modelling the impinging jet flow.

Keywords: downburst; speed-up; topography; impinging jet.

1. Introduction

A thunderstorm downburst is a strong downdraft which induces an outburst of potentially damaging winds on or near the ground (Fujita 1985, 1990). Downburst winds can be sub-divided into two event types; the microburst, with damaging wind extending less than 4 km, and lasting only a few minutes, and the macroburst with damaging winds extending greater than 4 km, and lasting between 5 and 30 minutes (Fujita 1985). Through meteorological studies such as the Joint Airport Weather Studies (JAWS), the Northern Illinois Meteorological Research on Downburst (NIMROD) (Fujita 1985, Hjelmfelt 1988), the Thunderstorm Outflow Experiment (Gast and

† Corresponding Author, E-mail: m.mason@civil.usyd.edu.au

Schroeder 2003), and the Thunderstorm Winds Project (Choi 2004), it is known that convective downdrafts, of which the downburst is one type, produce near-surface wind profiles that differ significantly from boundary layer wind profiles currently specified in design loading standards around the world. It is also recognised that in many parts of Australia, and in all likelihood most sub-tropical areas of the world, thunderstorm winds, and not synoptic winds, are responsible for the mid to high return period design wind speeds measured at 10 m above ground level (Holmes 2003). Synoptic winds however generally still govern low return period design due to the small temporal and spatial extent of high strength downburst events. Understanding the difference between downburst and boundary layer wind profiles is of interest for designers of both low- and high-rise buildings (Chay and Letchford 2002), as well as for the design of structures of large lateral extent (e.g. transmission line networks), where the possible differing correlation characteristics are important.

Downbursts have been modelled both numerically (e.g. Proctor 1988, 1989, Hjelmfelt, *et al*. 1989, Anderson, *et al*. 1992, Orf, *et al*. 1996, Orf and Anderson 1999) by the atmospheric science community, and experimentally (e.g. Fujita 1986, Lundgren, *et al*. 1992, Alahyari and Longmire 1995, Yao and Lundgren 1996, Holmes 1992, Wood, *et al*. 2001, Chay and Letchford 2002, Letchford and Chay 2002, Mason, *et al*. 2005, Lin and Savory 2006) by both the atmospheric science and engineering communities. For simplicity, the models typically used by those in the wind engineering community (Lin and Savory 2006 is an exception) have been of an impinging air jet, shown by Hjelmfelt (1988) to compare well with full-scale measurements. Researchers (Kim and Hangan 2007, Mason, *et al*. 2007) have also used numerical methods to model the more complex characteristics of an impinging jet for which physical experimentation has proven to be restrictive.

It has been shown by Selvam and Holmes (1992), Holmes (1992), Letchford and Illidge (1999), and Wood, *et al*. (2001) that the differing flow structure of ABL and simulated downburst flow produce differing topographic amplification effects for embankment type features. This paper seeks to extend these works to study the differing amplification effects observed for flow over a variety of topographic shapes (escarpment, triangular hill, and bell-shaped hill), sizes, and slopes. A comparison between amplifications due to simulated downburst flow over differing topographic features is also made. Downburst flow simulation has been performed using a steady flow impinging air jet model. It is understood that this engineering model fails to simulate all atmospheric parameters of a full-scale downburst, however for a generic model where the interest lies in producing possible mean and peak values, not reproducing a specific full-scale event, the pressure driven air jet is considered suitable. This model represents a long duration downburst for which the ring vortex/gust front is well removed from the impingement region. This model is the first step in a systematic analysis of the impinging jet/downburst model, and produces a "baseline" set of results for unsteady simulations to be compared with in the future.

Results for both numerical and experimental tests are presented, with the experimental results serving as validation for the numerical implementation of the model. With this validation, further use of the numerical model is justified without explicit experimental validation. This paper also details numerical results using several turbulence models (closure schemes) highlighting the possible inaccuracies in numerical modelling of impinging jets, and discusses the selection of a suitable scheme for minimising these errors. In the following section the test setups are explained for both the numerical and experimental simulations. The test results are presented in Section 3, which is split into three main sections: Turbulence model selection, Wall jet structure, and Topographic effects. Section 4 draws conclusions from the tests performed and discusses the implications for structural design and the usefulness of both numerical and experimental test procedures.

2. Test setup and methodology

2.1. Numerical setup

2.1.1. Flow solver

All numerical simulations were carried out with the commercial CFD solver, ANSYS CFX11 (ANSYS 2007). CFX11 is based on a coupled finite volume solver for the mass and momentum (and energy if required) equations. The numerical scheme is a co-located pressure based method which utilizes a modified Rhie-Chow algorithm to avoid decoupling. The resulting algebraic equations are solved by an algebraic multi-grid method. All velocity calculations use a 2nd order bounded differencing scheme while a 1st order upwind scheme is implemented for the convective terms in the turbulence equations, and a 2nd order scheme is used for all diffusive terms.

2.1.2. Geometry and boundary conditions

The flow being modelled is that of a stationary, steady flow, impinging air jet with a jet Reynolds number of approximately 70,000 based on the diameter of the jet and spatially averaged mean jet velocity. The computational domain is shown in Fig. 1 and is 5D long and 2.5D high, based on a jet diameter (D) of 0.104 m. The jet outlet was set at 2D above the impingement surface, a value which corresponds to average cloud height to downdraft diameter ratio observations given for the JAWS microbursts (Hjelmfelt 1988). Since the flow is steady and axisymmetric it was possible to perform a 2D simulation using a 2° sector of the geometry.

The three tested topographical features, escarpment, triangular hill, and bell-shaped hill are also shown in Fig 1. Eq. (1) was used to determine the bell-shape, after Bowen (1983), where h_{bell} is the local elevation of the topographic feature, H represents the crest height; x_{cr} represents the radial distance from the crest, and L_u is the radial distance to the point where $h_{bell} = H/2$. For the simulations reported in Sections 3.1 and 3.2, the topographic feature was removed and a simple flat impingement surface was used. For numerical tests in Section 3.3, simulations were carried out with each topographic feature crest located at x/D = 1.0 (Fig. 1) and x/D = 1.5. Two topographic heights were tested for the radial position of x/D = 1.0, H/D = 0.048 (5 mm) and H/D = 0.024 (2.5 mm), with only the larger feature being modelled at x/D = 1.5. Two topographic slope values were tested for each feature, Φ = 0.2 and Φ = 0.5, calculated as per AS/NZS1170.02 (Standards Australia 2002),

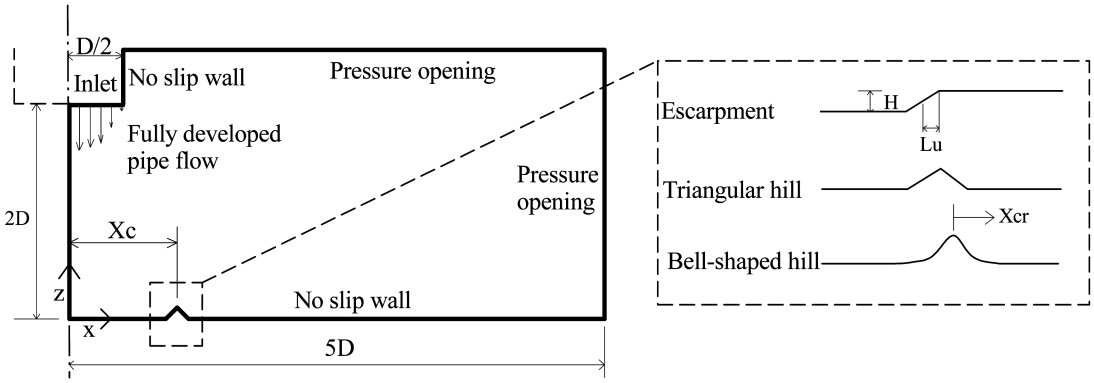

Fig. 1 Numerical geometry, boundary conditions, and topographic features tested

Eq. (2). These two slope angles were chosen so that comparison could be made with previous literature on impinging jet and boundary layer flows, and to study the difference in flow pattern between what could be considered shallow ($\Phi = 0.2$) and steep ($\Phi = 0.5$) slopes. It was expected that only a small separation region would occur behind the shallow slope features, while a larger separation region would exist behind the steep topographic features. The significance of this is that the numerical model is tested in both essentially attached flow, and largely separated flow regimes.

$$h_{bell} = \frac{H}{1 + \left(\frac{x_{cr}}{L_u}\right)^2} \tag{1}$$

$$\Phi = \frac{H}{2 \cdot L_u} \tag{2}$$

The computational mesh used varied depending on the test setup. For the geometry with no topographic features, a non-isotropic $400 \times 400 \times 1$ (peak $y^+ < 1.0$) mesh that increased in size with increasing distance from both the ground plane and the jet centre line was found to be sufficient to give mesh independent solutions. Mesh independence was assessed using velocity and k (turbulence kinetic energy) profiles along the impingement surface. A significantly larger number (twice as many in some cases) of mesh elements were required for mesh independence when topographic features were included, with particular grid refinement required around expected regions of flow separation.

The velocity, turbulent kinetic energy, k, and turbulence energy dissipation, ε, were set at the domain inlet. The velocity and k values were taken from experimentation (refer Section 2.2) and ε values were taken from a fully-developed numerical pipe flow simulation. A separate numerical simulation was used to determine the inlet ε condition due to the notorious difficulty in experimental measurement of this value. The top and side boundaries were set as pressure openings, these boundaries allow flow to either enter or leave the domain based on an assigned relative pressure (zero in this case). The two sides of the sector were set as symmetry boundaries. The ground was treated as a no-slip smooth wall, with the modelling of flow near the wall to be further explained in Section 2.1.3. The fact that the ground plane is treated as a smooth surface implies that no surface roughness effects have been included.

2.1.3. Turbulence models and their near wall characteristics

The aim of Section 3.1 is to determine which turbulence model is most appropriate for numerical impinging jet flow simulation. This section briefly details the turbulence models to be compared and the way the solver deals with each model near the wall. The great advantage of using a commercial CFD code for a study such as this is the large number of high quality, globally validated, turbulence models that can be implemented with relative ease. For this research six turbulence models were chosen to be compared, of which four were eddy-viscosity models and two were Reynolds stress models. Table 1 lists all six models tested along with the type of closure scheme and also the near-wall treatment employed. For a full numerical description of each model the reader is referred to ANSYS (2007).

The four eddy viscosity models used have been derived based on the assumption that the Reynolds stresses are proportional to the mean velocity gradients. Each model differs in exactly how this assumption is applied, and their basic concepts are as follows. The standard k-ε model is a

Table 1 Turbulence model type and near-wall treatmen

Model	Model type	Near-wall treatment
k-ε	Eddy viscosity	Wall function
k-ω	Eddy viscosity	Wall function and sub-layer treatment
RNG-k-ε	Eddy viscosity	Wall function
SST	Eddy viscosity	Wall function and sub-layer treatment
LRR-RSM	Reynolds stress	Wall function
BSL-RSM	Reynolds stress	Wall function and sub-layer treatment

semi-empirical model based on transport equations for k and ε (Launder and Spalding 1974). This closure scheme is only valid for fully turbulent flows and has been widely validated for many such cases. The k-ε model has however been shown to perform reasonably poorly for impinging jet studies due to an overestimation (up to four times experimental values) of turbulence produced in the impingement region (Craft, *et al*. 1993). Despite this fact the k-ε was included in our study as it is one of the most widely used models for industrial and wind engineering applications. The k-ω model is based on the model developed by Wilcox (1986) and solves two transport equations, one for k and a second for ω (turbulent eddy frequency). The advantage of using a turbulence model based on ω is that flow can be resolved all the way to a boundary (through the viscous sub-layer) without the use of non-linear damping functions. The k-ω model used also incorporates a limiter to the production of k in stagnation regions. When considering an impinging jet, and the fact that the ensuing wall jet is essentially driven by a large stagnation region, this limiter becomes important to the success of a model. The RNG (renormalisation group) k-ε model is essentially the same as the standard k-ε model, except for a change to a model constant (Yakhot, *et al*. 1992). Though this change sounds trivial, the variation in results is shown to be significant. The *RNG* k-ε model was used by Chay, *et al*. (2006) for three dimensional impinging jet/downburst modelling. The *SST* (Shear Stress Transport) model combines the k-ε and the k-ω models by way of a blending function (Menter 1994). The blending function ensures that the k-ε model is used in the free shear region, while the k-ω model is used near walls so the flow is resolved through the viscous sub-layer. This blending allows both models to work in the region of flow where they perform best (Menter 1994). The *SST* model also includes a second limiter (in addition to the one applied to the standard k-ω model) which provides an upper limit to the calculated eddy-viscosity, so that the transport of turbulent shear stress is modelled more accurately. The *SST* model was shown by Vieser, *et al*. (2004) to perform well for impinging jet simulations when compared with the k-ε model.

The two Reynolds stress models do not make the assumption of proportionality between Reynolds stress and mean velocity gradient. Instead these models solve additional transport equation for each of the unknown stresses along with a transport equation for ε or ω. The first model is the LRR (Launder Reece Rodi) Reynolds stress model developed by Launder, *et al*. (1975) and represents what could be considered a standard Reynolds stress model solving for ε. The second model is the BSL (Baseline) model, which behaves in a similar fashion to the *SST* model in that it switches from an ε based model in the free shear region to an ω based model in the near wall region. This again allows the flow to be resolved into the sub-layer for hopefully a more accurate set of results. Craft, *et al*. (1993) presented mean and fluctuating velocity profiles for impinging jet flow calculated with a standard Reynolds stress model and also a tailored (additional wall reflection correction) Reynolds

stress model. Results for the standard model compared poorly with experimental data; however the model with the wall reflection term performed well. The numerical impinging jet/downburst model of Kim and Hangan (2007) also used a Reynolds stress model that included a wall reflection term which gave reasonable results. In this research, generic models that do not include problem specific wall reflection terms were used, as these terms are not included in ANSYS CFX11.

When flow of any kind approaches a solid boundary, the general assumption that the flow is fully turbulent breaks down, thus special treatment must be afforded to these regions. The wall function treatment used for turbulence models solving an ε equation is an extension of the method of Launder and Spalding (1974). This function uses a logarithmic relation for the velocity at the near-wall node, where the fully-turbulent assumptions made by the turbulence models do not apply. To avoid issues associated with mesh refinement near the ground plane, which may bring the first near-wall node into the viscous sub-layer, the near-wall treatment ensures that calculations are not made for nodes below a specified sub-layer/log-law interaction point (y^+ = 11.08 used) (ANSYS 2007). This treatment meant that the very fine near wall meshes used for ω based models could be used for the ε based models without problems occurring in the viscous sub-layer. For models involving an ω equation a low Reynolds number formulation is possible in the viscous sub-layer region, based on an analytical expression (Wilcox 1986), thus resolving the flow to the solid boundary. An automatic treatment exists that switches between the wall function described above and the low Reynolds number formulation if the first computational node lies in the laminar sub-layer. This near-wall formulation therefore includes the laminar sub-layer in the mass and momentum balances (ANSYS 2007), therefore reducing the error in calculations of boundary layer growth. Again, for numerical descriptions of the near wall treatment described above, refer to ANSYS (2007).

2.2. Experimental setup

Validation for the numerical results was undertaken at the School of Civil Engineering Impinging Jet Facility within The University of Sydney. The facility has a 0.104 m diameter circular plastic pipe which runs uninterrupted for 6 m (58D) and expels air onto a smooth (sheet metal) impingement surface 0.208 m (z/D = 2.0) from the outlet, Fig. 2. The 58D length of pipe is long enough to obtain fully developed velocity and turbulence profiles which compare well with data from experiments by Laufer (1954). The flow conditions preceding the pipe are the same as given in Wood, *et al*. (2001). The air jet was run so that the spatially averaged velocity (W_{bulk}) through the

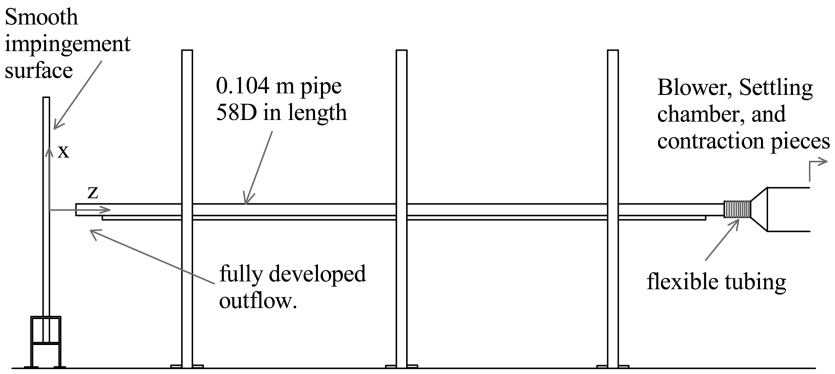

Fig. 2 Experimental impinging jet facility

pipe was 10 m/s (Re = 70,000) with a centre-line mean velocity (W_{CL}), measured at the jet outlet, of approximately 12 m/s. The impingement surface was covered with smooth sheet metal so that the hydraulically smooth surface modelled numerically could be replicated. The topographic features tested are shown in Fig. 1, and were all two dimensional in nature. For experimental validation the features were only tested extensively with H = 5 mm and positioned with the crest at x/D = 1.0, however some isolated tests were carried out for other feature configurations as required. Features were made from finely sanded timber; thus the roughness characteristics were slightly different to that of the impingement surface but were still classified as hydraulically smooth.

Velocity and k profiling was performed with a 4-hole cobra probe or a single wire thermal anemometer (hot-wire) sampled at 1250 Hz for 30 seconds. Velocity and turbulence comparisons between the cobra probe and the hot-wire anemometer showed the cobra probe to be suitable for use down to 2 mm (measured to centre of probe) from the surface when the flow was not influenced by a large separation region. Along the flat surface and above the crest of each topographic feature, measurements below 2 mm were made with a hot-wire anemometer to overcome deficiencies of the cobra probe. Hot-wires were also used for velocity measurements where high gradients exist near the lee slope vortex, as the cobra probe was found to be unsuitable in this region. The cobra probe was still used for larger elevations however, as it measured velocity fluctuations in three dimensions which allowed an experimental measurement of k. The accuracy of the cobra probe, as reported by Mousley (2002), is 0.2 m/s within the range 2 m/s – 30 m/s. It is therefore deduced that the accuracy of the mean velocity readings in the lower part of the profile (highest velocities) are expected to be within ± 4% of their true value. These accuracies are for velocities above 2 m/s; in this study any measurements using the cobra probe below this threshold have been discarded. Additional inaccuracies will also arise due to a positioning error, and there is also an averaging error over the faces for the cobra probe. These errors also will vary throughout the test domain and are primarily caused by the velocity gradients. Hot-wire measurements in the same region are expected to have an accuracy of approximately 2%. The turbulence kinetic energy, since only measured by the cobra probe, has a corresponding expected accuracy to within ±14%.

3. Results

This section is split into three parts: Section 3.1 details the performance of the turbulence models described in Section 2.1.3 by comparing velocity and k profiles with experimental data; Section 3.2 compares experimental velocity profiles for a larger number of radial positions with the numerical results using the most appropriate turbulence closure scheme. Section 3.2 also compares velocity profiles with full-scale downburst measurements, atmospheric models, and suggested codification. Section 3.3 then shows the effect on the velocity profiles of the three topographic features. The results are presented as both normalised velocities and topographic multipliers, as the latter is the current practice for dealing with topography in design standards. Presenting the effects of topography as multipliers also allows direct comparison with different sized features, and published work on topographic effects in simulated downbursts and boundary layer wind fields.

3.1. Turbulence model selection

Fig. 3 shows a comparison between experimental and numerical velocity profiles measured at (a) x/D = 0.65, (b) x/D = 1.0 and (c) x/D = 1.5. This radial range encompasses the region of peak

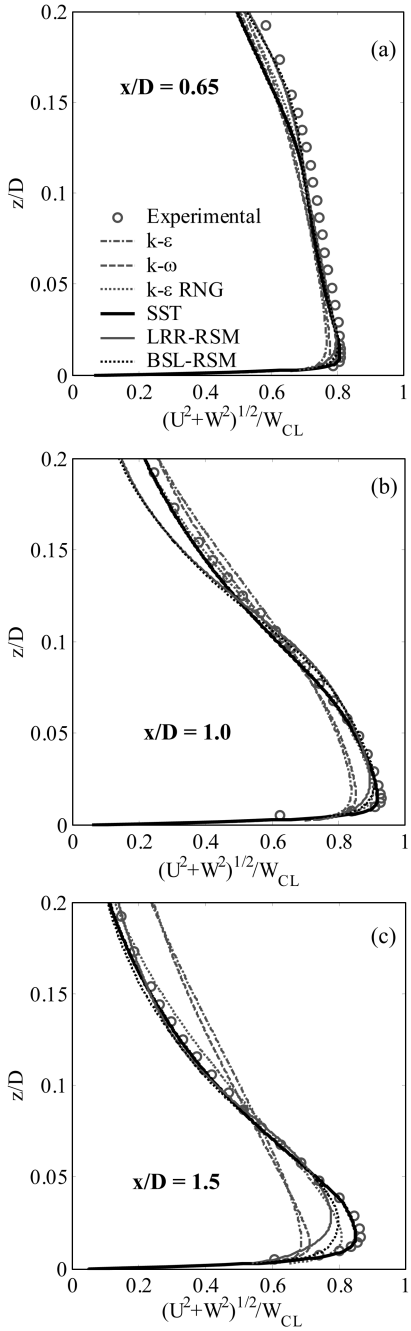

Fig. 3 Development of normalised velocity profile along the impingement surface

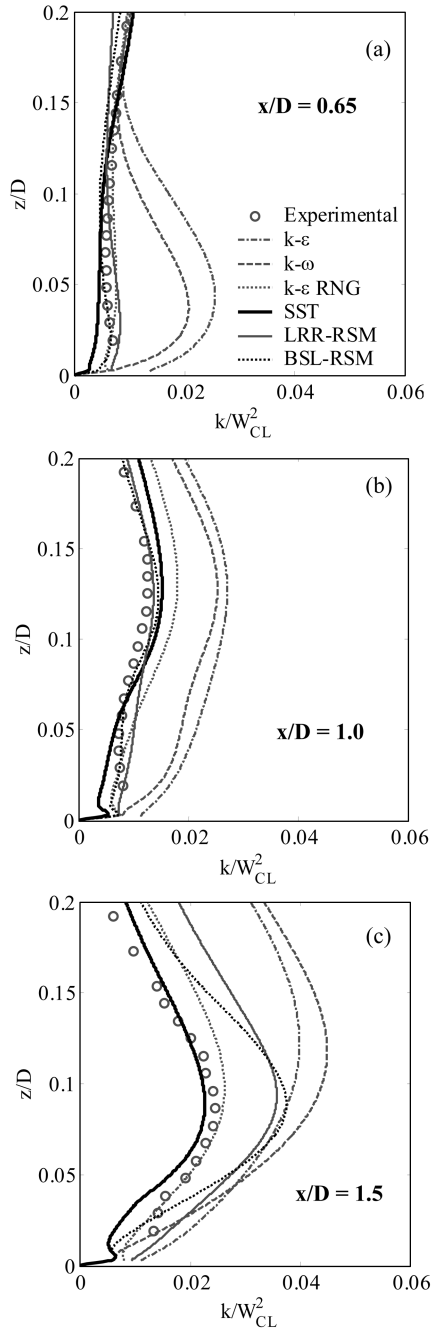

Fig. 4 Development of normalised k along the impingement surface

velocities which are of importance when considering peak loading for design. From an impinging jet standpoint, this region is part of the development region where the impinging flow is being turned and is developing into a self-similar wall jet. Wood, *et al*. (2001) suggest that after x/D = 1.5

the wall jet has stabilised to a point where a single normalised profile is representative. Before this point however, the velocity profile is highly variable with respect to the radial position. Elevation from the impingement surface (z), shown on the ordinate, has been normalised against D, while velocities, shown on the abscissa, have been normalised against the time averaged jet centre line velocity, W_{CL}. Velocities are shown as the resultant of the U and W components (parallel and perpendicular to the wall, respectively) so that hot-wire and cobra probe data could be shown concurrently. It should be noted however that the contribution of W is less than 5% for all elevations for $x/D > 0.8$.

Fig. 3(a), $x/D = 0.65$, shows for the region close to impingement a slightly decreasing velocity profile is produced up to an elevation of $z/D \sim 0.15$, after which point the velocity drops off much more rapidly with elevation. It is also evident that there are only small differences between the velocity results obtained by different closure schemes, with generally less than 10% separating values at any given elevation. When the numerical results are compared with the experimental results, it is evident the numerical models predict the experimental results shape well, but with a marginal under prediction of magnitude.

As the jet expands differences begin to appear between the numerically predicted velocity profiles. At $x/D = 1.0$, Fig. 3(b), the location of the largest recorded mean velocity, the k-ε and k-ω closure schemes clearly under-predict the experimental velocities at low levels with a minor over-prediction with increased z/D. The two Reynolds Stress models marginally under-predict velocities at low levels ($z/d < 0.025$), over-predict velocities up to $z/D \sim 0.1$, and again under-predict values above this elevation. The closure schemes which produce the best replications of the experimental velocity profiles are the *SST* and *RNG* k-ε models. The *SST* model in particular follows the experimental results extremely well with only a slight underestimation at higher levels. The *RNG* k-ε model marginally under-predicts results below $z/D = 0.05$.

As the jet expands further, Fig. 3(c), all closure schemes appear to under-predict velocities at the lower levels, however the SST model does appreciably better than all other closures. The simple k-ε and k-ω models again produce the poorest results as they fail to predict the development of the boundary layer properly.

Fig. 4 compares the values of k obtained numerically with those measured experimentally at the same radial positions as Fig. 3. The ordinate is again normalised against the jet diameter D, while the abscissa is normalised against the square of the centre line velocity, W_{CL}^2. As the flow is turned near the impingement point, Fig. 4(a), the experimental values show a gradually increasing trend in k with increasing elevation. The peak in k occurs between $z/D = 0.2$ and $z/D = 0.3$ (above figure limits) and is associated with the shear layer produced between the jet and the initially stationary ambient air. Again the k-ε and k-ω models produce poor results, particularly at low elevations where the magnitude predicted is in excess of four times that measured. This poor performance has previously been reported (Launder and Sandham 2002, Craft, *et al*. 1993). The remaining models better predict the k profile magnitude and shape. At $x/D = 1.0$, Fig. 4(b), the peak in k occurs between 0.1 z/D 0.15 and is roughly the same magnitude as that for $x/D = 0.65$. Again, this is the shear layer between the two flow regimes. All turbulence models predict the shape of k reasonably well but typically slightly overestimate the magnitude. At $x/D = 1.5$, Fig. 4(c), the peak in k has moved below $z/D = 0.1$ and has doubled in magnitude over an x/D range of $0.5D$. A clear distinction is evident between all turbulence models at this radial position. The k-ω model gave the worst prediction with a peak k value double that measured. The SST model predicted a reasonably accurate peak value of k while also predicting the elevation of the peak correctly.

The reason that different turbulence models give such different results for impinging jet flow is because the turbulence mechanisms present near impingement vary significantly from those in simple shear flows for which general turbulence models have been developed (Launder and Sandham 2002). Using the relatively poor performance of the k-ε model as an example, Yap (1987) shows how the assumptions of the equilibrium boundary layer breakdown for the non-equilibrium impingement region and produce length scales, and thus k values, many times the measured size. Yap (1987) proposed a "damping" term that limits the calculated length-scale by increasing the value of ε; this correction was shown to improve heat transfer predictions, which in essence means an improved prediction of k has occurred. A similar "damping" term is present in the *SST* closure scheme where a limiter is applied to the creation of eddy viscosity (linked to k). This limiter stops the build up of k in the impingement region and allows shear stresses to be transported throughout the domain, thus leading to more accurate results. A similar limiter is used in the *v2f* model which Vieser, *et al*. (2004) showed gave comparable results to the *SST* model.

From the data presented above it was concluded that the *SST* model was the most suitable for modelling steady impinging jet flows from the available models in CFX11. Therefore all subsequent numerical results are based on this formulation. The Reynolds stress models available in CFX11 were believed to perform poorly, when compared with results presented in Craft, *et al*. (1993) and Kim and Hangan (2007), due to the absence of wall reflection terms.

3.2. Wall jet structure

The structure of a steady impinging jet is relatively well-reported in the wind engineering community, e.g., Wood, *et al*. (2001), Chay, *et al*. (2006). It should be noted however that the velocity profile shape and development will vary depending on the impinging jet used, thus the applicability of the jet outlet characteristics to real downburst situations must be considered. It is considered that since atmospheric modellers (Proctor 1988, Orf, *et al*. 1996) prescribe temperature or water profiles that lead to a velocity profile which decreases with distance from the downdraft centre, the developed pipe flow profiles used herein is a reasonable approximation of a possible downdraft type. The relatively constant outlet velocity profile approach taken by Mason, *et al*. (2005) and Kim and Hangan (2007) is an equally valid representation of a profile that could exist.

Velocity profiles for the range $0.65 \le x/D \le 2.0$ are shown in Fig. 5, again normalised against the time averaged jet centre line velocity, W_{CL}. Profiles are presented in a format so the variability in shape can be observed as a function of radial position. Each profile begins with a normalised velocity of 0.0 at its specified radial position (i.e. $(U^2+W^2)^{½}/ W_{CL} = 0$ for a radial position of x/D = 1.0 at x/D = 1.0 on the abscissa) thus the abscissa can be read as a velocity scaled by the relationship $\{x/D = 0.5\} = \{(U^2+W^2)^{½}/W_{CL} = 2\}$. The wall jet component of the flow starts with a relatively uniform velocity profile with elevation and as the flow is turned through impingement the profile tends to become more "nose" shaped. A maximum mean velocity magnitude is reached between x/D = 1.0 and x/D = 1.2. As the radial location increases past this maximum, the relative magnitude of the velocity profile decreases as momentum is lost through mixing with surrounding air, and three dimensional divergence spreading the jet over an increasing area (radial expansion).

For a single elevation, say the elevation of peak velocity, the velocity increase to the radial point of maximum velocity is essentially linear with a slower tailing decrease after that point. Hjelmfelt (1988) shows a similar trend for 8 full-scale JAWS microbursts near the time of maximum intensity but they exhibit a much quicker decay after the peak. Hjelmfelt (1988) suggests the reason for this

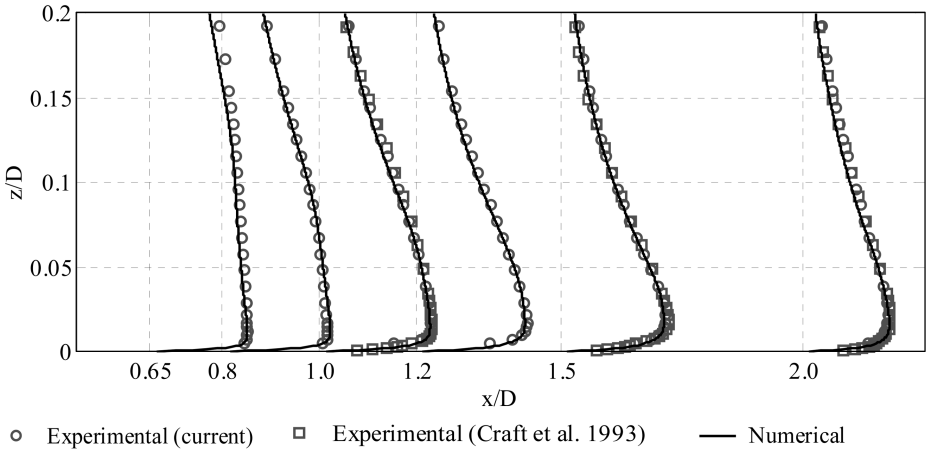

Fig. 5 Radial development of normalised velocity profile; a comparison between numerical (*SST*), our experimental, and previous experimental (Craft, *et al*. 1993) work. Note, An *x*/*D* range of 0.5 scales to a value of $(U^2+W^2)^{½}/W_{CL} = 2$

discrepancy is that the steady flow impinging jet has the leading edge well removed from the region of peak winds (i.e. it is simulating an outflow that has been impinging the ground for an extended period of time), while the full-scale cases generally produce peak winds soon after the leading edge of the downburst impinges the surface. This is a major problem with the steady impinging jet model when trying to model for peak loads that typically occur near the front of an outflow, however its applicability to long duration downbursts or gravity currents (where the peak occurs due to the quasi-steady impingement region, Proctor (1988)), is more realistic. It is also clear from Fig. 5 that a boundary layer develops as the flow moves away from the impingement zone, which suggests that surface roughness will play a role in the development of the velocity profile. Preliminary results on this topic, presented in Hangan and Xu (2005), suggest that increases in surface roughness tend to increase the elevation of maximum velocity in a particular profile.

Hjelmfelt (1988) in the analysis of JAWS microbursts gives velocity profiles (maxima at each elevation for flow parallel to the ground over all radial positions) for several microburst events. The upper and lower bounds of these results are compared with the experimental and numerically predicted radially independent maximum mean velocity results for our test set. As well as the JAWS results, Fig. 6 shows full-scale data from the NIMROD project (Fujita 1981), the Singapore Thunderstorm Wind Project (Choi 2004), the analytical downburst model of Oseguera and Bowles (1988) further developed by Vicroy (1991), and the codification suggestion of Holmes, *et al*. (2005), which is based on the work of Oseguera and Bowles (1988). The codification example uses equation parameters given in Holmes, *et al.* (2005) that may be changed to alter the profile shape. The data used from Choi (2004) is for a type II (high wind speeds occurring at low elevations) event. The numerical and experimental results shown provide a good approximation to the upper bound of full-scale data, which from a design perspective is attractive when a conservative design approach is desired. It was found that for higher elevations ($z/D > 0.08$), not shown in Fig. 6, and very low elevations ($z/D < 0.01$), the radially independent maxima for a given elevation occurs close to the impingement point, i.e., $x/D < 1.0$. For the region $0.01 < z/D < 0.08$ however the maxima occurs at approximately $z/D = 1.0$. This suggests that from a codification perspective, a velocity profile taken at a single radial position (say $x/D = 1.0$) may not be entirely conservative.

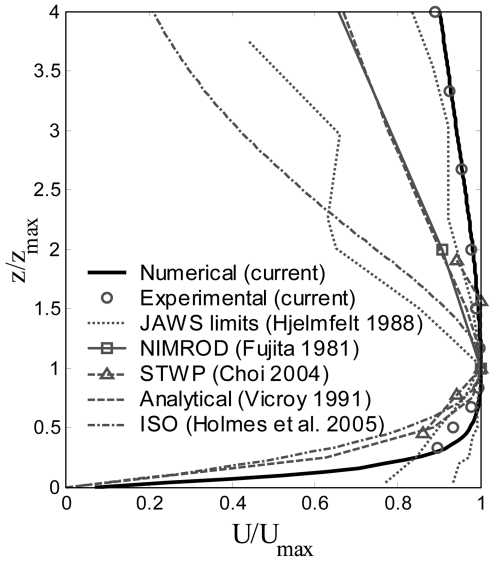

Fig. 6 Comparison between numerical results and a range of full-scale and analytical results

3.3. Topographic effects

Three topographic features were tested for this research; an escarpment, a triangular hill and a bell-shaped hill, Fig. 1. All were two dimensional features located at radial positions of $x_c = 1.0D$ or $x_c = 1.5D$, with a height (H) of $0.048D$ (5 mm) or $0.024D$ (2.5 mm). Experimental validation of the numerical model was carried out for all features with parameters, $x_c = 1.0D$ and $H = 0.048D$, all other tests, though not explicitly validated, were assumed to have similar accuracy to the validation cases. Some additional experimental tests were carried out for further validation described throughout this section. The location of $x_c = 1.0D$ was chosen for primary validation as this corresponds with the location of maximum measured mean velocity over a flat impingement surface. The height, H, of $0.048D$ was chosen as it corresponds to a scaled topographic feature of 50 to 100 m (based on a downdraft diameter of 1 to 2 km). Differing radial crest positions (x_c) were studied to determine if topographic speed-up varied with velocity profile, and different feature heights were studied to determine the influence of the wall jet thickness (δ) (δ measured to the elevation of $U_{max}/2$, above U_{max}) on this speed-up.

3.3.1. Mean velocity profiles

Fig. 7 shows measured and predicted mean velocity profiles over the six topographic features with each crest located at $x_c = 1.0D$. Fig. 7(a) shows results for the escarpments, Fig. 7(b) for the triangular hills, and Fig. 7(c) for the bell-shaped hills. A summary of selected results measured and predicted above the crests are presented numerically in Table 2 (a rough scaling of $D = 1000$ m can be used for full-scale conversion). Three velocity profiles were measured for each topographic setup, one at the crest and then two behind the crest at $+1H$ ($x = x_c + 1H$) and $+2H$ ($x = x_c + 2H$). This range allowed an assessment of the numerical model at the point of typical maximum amplification, the crest, and in separated flow regions. All elevations are normalised against H, while velocities are normalised against the time averaged jet centre line velocity, W_{CL}. Mean velocities can

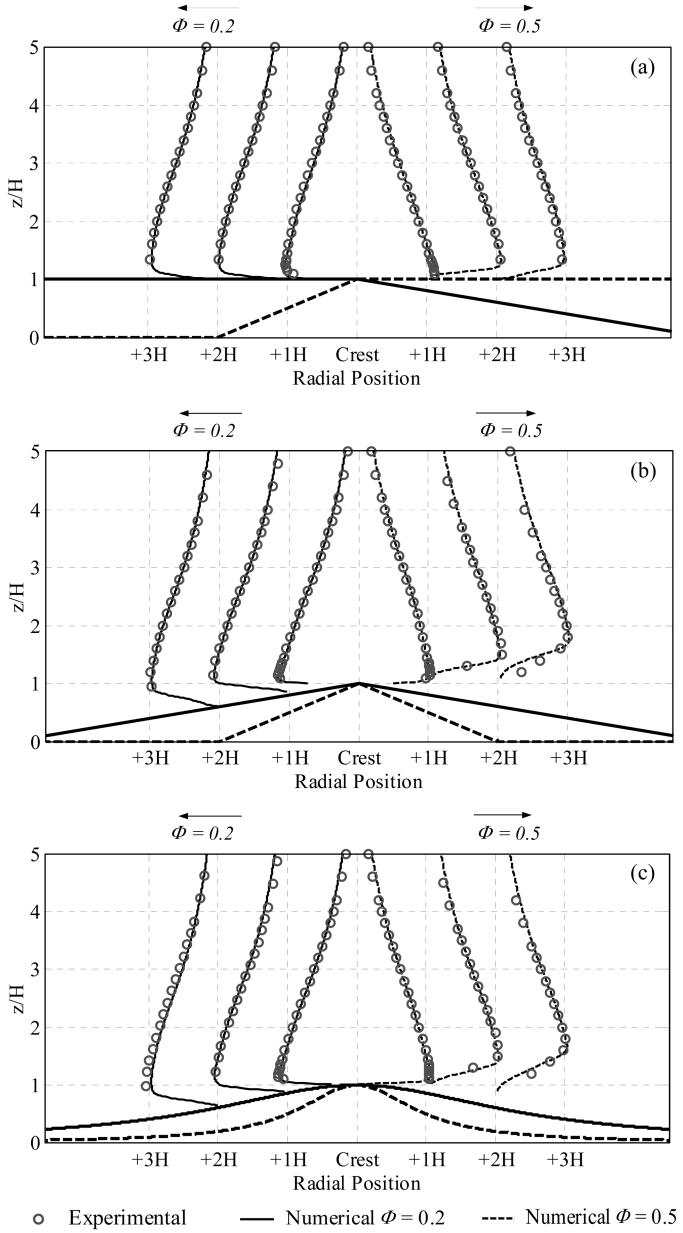

Fig. 7 Velocity profiles over topographic features with slopes of $\Phi = 0.2$ and $\Phi = 0.5$. (a) escarpment, (b) triangular hill, and (c) bell-shaped hill. Note, $1H = \{(U^2+W^2)^{½}/W_{CL} = 1\}$

be measured along the abscissa by the relationship, $1H = \{(U^2+W^2)^{½}/W_{CL} = 1\}$. Results for both the shallow ($\Phi = 0.2$) and steep ($\Phi = 0.5$) cases are given on the same plot with the shallow and steep slope profiles shown on the left and right hand sides, respectively. For further distinction the shallow slope (surface and velocity profile) is plotted as a solid line while the steep slope is plotted as a dotted line. All velocity profiles start with a value of $(U^2+W^2)^{½}/W_{CL} = 0$ at their specified radial position and increase in the direction of increasing x. Only positive values have been displayed on the figures

Table 2 Normalised velocity values, numerical and experimental (within parenthesis), above the crest of each topographic feature

z/D	Flat surface	Escarpment $\Phi = 0.2$	Escarpment $\Phi = 0.5$	Triangular hill $\Phi = 0.2$	Triangular hill $\Phi = 0.5$	Bell-shaped hill $\Phi = 0.2$	Bell-shaped hill $\Phi = 0.5$
0.01	0.92 (0.91)	1.05 (1.02)	1.13 (1.10)	1.14 (1.14)	1.01 (1.02)	1.12 (1.13)	1.07 (1.05)
0.02	0.92 (0.93)	1.02 (1.01)	1.08 (1.06)	1.09 (1.10)	1.00 (1.00)	1.09 (1.10)	1.04 (1.04)
0.03	0.91 (0.91)	0.97 (0.98)	1.00 (1.00)	1.02 (1.04)	0.95 (0.97)	1.02 (1.04)	0.98 (1.00)
0.05	0.86 (0.86)	0.89 (0.91)	0.89 (0.89)	0.91 (0.91)	0.88 (0.89)	0.91 (0.93)	0.89 (0.90)
0.07	0.79 (0.78)	0.79 (0.82)	0.79 (0.78)	0.80 (0.79)	0.80 (0.79)	0.80 (0.80)	0.80 (0.80)
0.10	0.64 (0.66)	0.62 (0.65)	0.61 (0.60)	0.60 (0.60)	0.64 (0.63)	0.61 (0.62)	0.63 (0.63)
0.14	0.40 (0.42)	0.37 (0.38)	0.36 (0.33)	0.35 (0.32)	0.39 (0.38)	0.36 (0.33)	0.39 (0.36)
Maximum	0.92 (0.93)	1.05 (1.03)	1.15 (1.12)	1.16 (1.15)	1.01 (1.02)	1.12 (1.13)	1.07 (1.05)

because experimental measurements were not possible in reverse flow, thus no direct comparison could be made between the results in this region. Therefore, if flow separation occurs and a vortex is formed, the numerical results will appear to stop before the surface.

For both the shallow and steep escarpments (Fig. 7(a)) the highest mean velocity is recorded above the crest with maximum normalised velocities of 1.05 (1.03) and 1.15 (1.12) respectively; numerical (experimental). For reference, the maximum normalised mean velocity over a flat surface at $x/D = 1.0$ is 0.92 (0.93). It is evident that the maximum mean velocity occurs at higher elevations away from the crest due to the presence of a small separation region, or the development of a boundary layer. It is also clear that the maximum occurs at lower elevations above the crest when compared to flow over the flat surface (Table 2); this will be further discussed later in this section. The numerical model shows excellent agreement with the experimental results at all locations. The largest discrepancy was less than 5%, suggesting that for features with little or no flow separation the numerical model is capable of producing accurate engineering flow predictions.

For the triangular hill presented in Fig. 7(b) two distinct regimes exist. For the shallow hill, only a small region of flow separation occurs leading to an almost constantly attached flow, while for the steep hill a large separation region develops behind the feature due to the formation of a large recirculating vortex. Looking firstly at flow over the shallow hill, an excellent numerical replication of experimental results is observed with differences again not exceeding a few percent. The maximum mean velocity is again observed above the crest with a normalised value of 1.16 (1.15), a magnitude similar to that for the steep escarpment. This similarity is in contrast with results for similar slope features in boundary layer flow for which Bowen and Lindley (1977) and Pearse, *et al*. (1981) showed a 10% increase in wind speed for the shallow triangular hill when compared with results over the steep escarpment. A marginally larger difference is prescribed in the Australian Standards (Standards Australia, 1989 – the 1989 standard is used as it was based on mean velocities).

For flow over the steep triangular hill it is evident by the rise in elevation of maximum velocity with increasing x that the flow is no longer attached to the lee surface of the hill and that a large separation vortex now exists. A good prediction of this flow field is produced with the numerical model, both over the crest, and in the lee down into the shear layer between the jet flow and the separation vortex. A maximum normalised mean velocity of 1.01 (1.02) is observed above the crest at an elevation of $z/D \sim 0.01$, a decrease in magnitude of approximately 15% from the shallow hill

case. This decrease is in stark contrast to what is observed in boundary layer flow, where an increase of a few percent from shallow to steep is expected (Pearse, *et al*. 1981). The Australian Standards even suggest an increase of over 15% (Standards Australia 1989). The reason this difference exists is because the non-confined nature of the wall jet does not force the lee flow to quickly reattach, and a correspondingly larger separation vortex forms. The lee vortex effectively reduces the angle that the flow is turned through (smaller effective slope), thus reducing the velocity speed-up. The effective slope is defined here as a measure of the localised curvature of the flow as it moves over the crest of a topographic feature. For example, if it is assumed that the flow stays attached over a $\Phi = 0.2$ slope triangular hill it must be turned through approximately 23° at the crest to reattach to the lee slope. If however a separation bubble forms behind the crest, which does not allow the flow to reattach immediately, the localised curvature may only be (say) 15° which would correspond to the curvature produced for fully attached flow over a slope with a smaller value of Φ, thus leading to a smaller effective slope. A similar effect has been observed for boundary layer flow (Pearse, *et al*. 1981) but the confined nature of the boundary layer means that the flow near the surface is not free to move in the same way vertically, thus creating a smaller separation region, a larger effective slope, and therefore a larger speed-up. For the two lee profiles the numerical model predicts the velocity field through the upper and shear layer regions reasonably well but appears to over predict values deep in the shear layer. It is however expected that for a non-stationary flow, such as a vortex, the hot-wire probe may be causing measurable disturbance to the flow, which is expected to be the reason for the divergence at this location. Another point of note is that the magnitude of the maximum velocity is maintained over the three measured profiles, unlike for $\Phi = 0.2$, where it decreases with distance from the peak. This occurs because the curvature of the flow over the steep hill remains reasonably constant up to $x/D = x_c + 2H$.

The bell-shaped hill, Fig. 7(c), shows similar results to those presented for the triangular hill with a maximum normalised velocity above the crest of 1.12 (1.13) for the shallow slope and 1.07 (1.05) for the steep slope. The maximum normalised velocity is a reduction from the value of 1.16 (1.15) reported for the triangular hill and is most likely due to the rounded crest leading to slightly reduced localised curvature of the flow. For the steep hill an increase in normalised velocity of approximately 5% was observed when compared with the triangular hill, this is believed to occur because the rounded nature of the hill meant that a smaller recirculation region formed in the lee, slightly increasing the effective slope. For the shallow slope the numerical model predicts the mean velocity profiles well at the crest and $+1H$, but slightly under-predicts values at $+2H$. For the steep slope, the same numerical trend was observed as for the triangular hill, where the profile over the crest is predicted well but the measurements deep in the shear layer show some discrepancies with numerical predictions. When comparing Fig. 7(b) and Fig. 7(c) the location of the shear layer is seen to be marginally lower for the bell-shaped hill than the triangular hill supporting the statement regarding the re-circulation size behind the feature.

Fig. 8 shows a mean velocity profile comparison between flow over a flat surface and flow above the crest for the three topographic features; Fig. 8(a) for the shallow, and Fig. 8(b) for the steep features. Axes are normalised as in Fig. 3. For both slope angles the topography is seen to increase the velocity magnitude compared with the flat surface for $z/D < 0.07$, or approximately $1.5H$, above which point the velocity is reduced. For the shallow topographic features the triangular hill produces the maximum mean velocity, followed by the bell-shaped hill, then finally the escarpment. For the steep features however the opposite trend is observed where the escarpment produces the maximum mean velocity while the triangular hill produces the smallest. As explained earlier in this section,

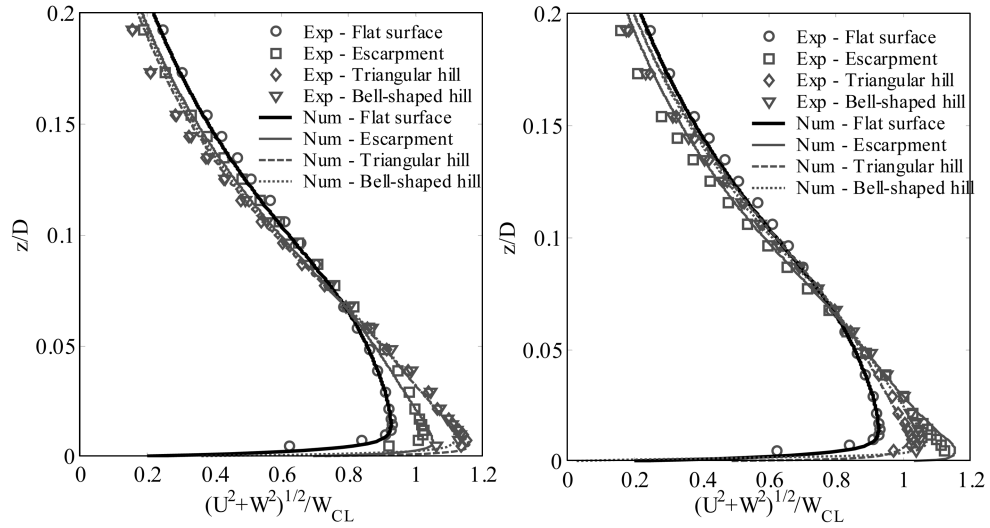

(a) Slope angle, $\Phi = 0.2$. (b) Slope angle, $\Phi = 0.5$.

Fig. 8 Velocity profiles measured over a flat surface (x/D = 1.0), and above the crest of topographic features, (a) $\Phi = 0.2$, and (b) $\Phi = 0.5$.

this difference is due to the differing characteristics of the separation region behind the steep topographic features and the level of re-attachment, and hence effective slope, that it allows.

Results presented suggest that the numerical model predicts the mean velocity profiles over topographic features when little or no separation occurs (escarpments or shallow hills) extremely well. The numerical model also predicts mean velocity profiles over the crest of steep hills well, but results begin to differ deep in the shear layer between the lifted wall jet and the re-circulation vortex in the lee of the hill. It is however believed that the lee discrepancy is due to the inability of the hot-wire to measure velocities within the vortex accurately. It was also shown that when large separation regions exist, the maximum mean velocity recorded above the crest is maintained to a radial position of +2H due to the maintenance of localised curvature.

3.3.2. Topographic multipliers

To enable a comparison between differing hill sizes, crest locations, and flow regimes, the velocity amplifications due to topographic features have been converted to topographic multipliers. The first multiplier discussed, M_t, is the standard form and is as described in Eq. (3). The second multiplier, $M_{t,\max}$, is an elevation independent representation of the maximum velocity amplification for a specific profile, as described in Eq. (4).

$$M_t = \frac{Velocity(z)_{topography}}{Velocity(z)_{flat}} \tag{3}$$

$$M_{t,\max} = \frac{max(Velocity(z)_{topography})}{max(Velocity(z)_{flat})} \tag{4}$$

$Velocity(z)_{topography}$ refers to the velocity measured at a specified elevation, z, above the local surface level, with velocity again being the resultant of the U and W components as previously used. Similarly $Velocity(z)_{flat}$ is the velocity measured at the same radial location with no

topographic features present. Measured and predicted $M_{t,\max}$ values are presented in Table 3 for flow above the crest. This multiplier gives an indication of the amplification of the maximum velocity while removing the multiplier dependence on the elevation at which it occurs. It is believed that $M_{t,\max}$ gives a better representation of true amplification for impinging jet flow, however from a design perspective M_t values may be more beneficial.

Fig. 9 presents a comparison between measured and predicted M_t values for the cases discussed in Fig. 7 ($x_c = 1.0D$; $H = 0.048D$ – large feature), predicted results for cases with a topographic feature half the size, ($x_c = 1.0D$; $H = 0.024D$ - small feature), and the cases with the crest located at $x_c =$ 1.5D ($x_c = 1.5$D; $H = 0.048$D). The abscissa indicates the radial position as well as the measurable quantity, in this case M_t. Again profiling is done from the solid surface line for $\Phi = 0.2$ and from the dotted surface line for $\Phi = 0.5$. For each radial position the given location corresponds to an M_t value of 1.0 (i.e. the vertical line directly above the crest corresponds to a value of $M_t = 1.0$ for the crest profile). M_t values increase in the direction of flow. M_t values above the crest for experimental and numerical simulations can be obtained for the large topographic feature positioned at $x_c = 1.0$ by dividing the given normalised velocity value in Table 2 by the corresponding value over the flat surface.

For both the shallow and steep escarpments, Fig. 9(a), the large and small features produce similar amplification profiles with the region below $1.5H$ above the local surface causing a velocity speed-up (refer to Fig. 8 for example). Upon close inspection it is seen that the small feature produces only marginally higher M_t values than the large feature, this indicates that an effective doubling of the relative wall jet thickness (H/δ) has a minimal effect on the amplification profile in this relatively attached flow. This finding supports the suggestion made by Letchford and Illidge (1999) that the ratio of topographic height to wall jet thickness does not greatly affect M_t profiles, based on a comparison with Holmes (1992). When comparing results at $x_c = 1.0D$ and $x_c = 1.5D$, again little difference is observed, which suggests that the radial position has little affect on the amplification ratios. This was also suggested by Wood, *et al*. (2001). This finding suggests that slight variations in both velocity and turbulence profiles have little affect on velocity amplification of flow over an escarpment where little flow separation occurs. The similarity between profiles is also echoed in the $M_{t,\max}$ values in Table 3 with less than a 5% variation between values over the same slope feature. Upon further inspection of Fig. 9(a), two types of profile are seen; one associated with flow over the crest, and the other associated with flow in the lee. The profile associated with the crest steadily increases with decreasing elevation to around $x/D = 0.02$, after which it rapidly increases. This can be explained by examination of Fig. 8 where the topographic feature is shown to not only increase velocity magnitude but also to decrease the elevation at which it occurs. The combination of these

Table 3 $M_{t,\max}$ values above the crest for all topographic features (experimental results in parentheses)

Topography type	Large topography $x_c = 1D$	Small topography $x_c = 1D$	Large topography $x_c = 1.5D$
Escarpment ($\Phi = 0.2$)	1.14 (1.10)	1.12	1.11
Escarpment ($\Phi = 0.5$)	1.26 (1.20)	1.21	1.23
Triangular hill ($\Phi = 0.2$)	1.26 (1.24)	1.16	1.21
Triangular hill ($\Phi = 0.5$)	1.11 (1.10)	1.11	1.09
Bell-shaped hill ($\Phi = 0.2$)	1.22 (1.22)	1.19	1.18
Bell-shaped hill ($\Phi = 0.5$)	1.16 (1.13)	1.13	1.12

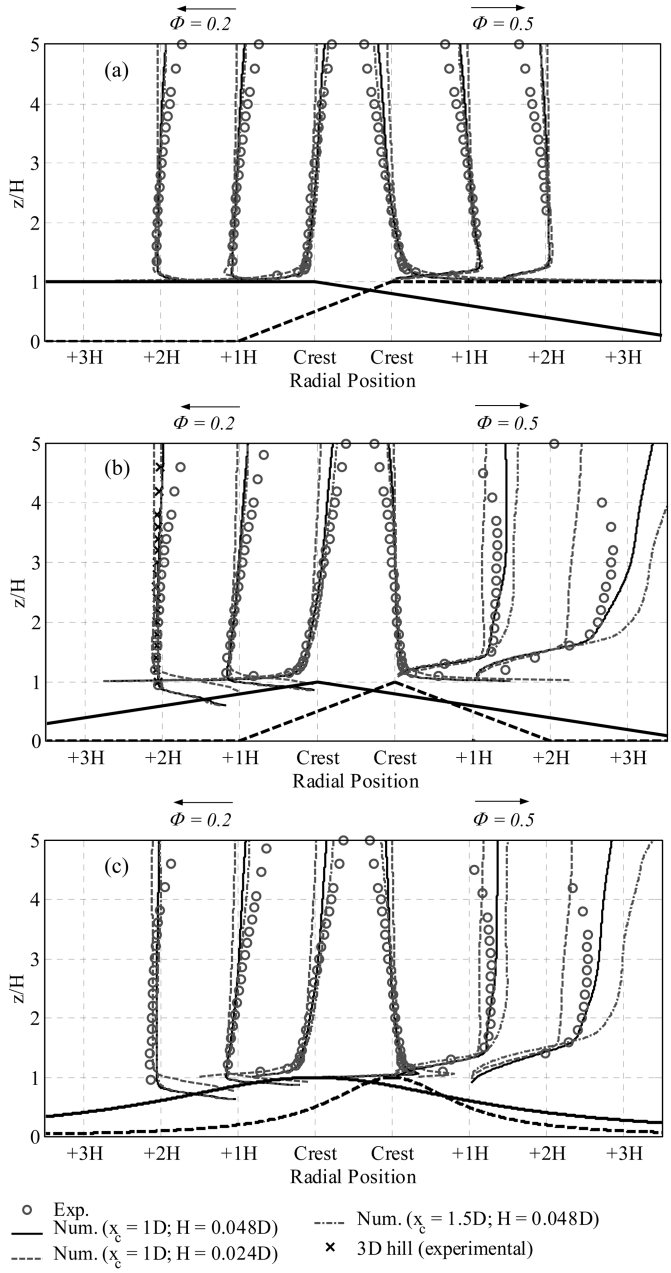

Fig. 9 Topographic multipliers for flow over topographic features, (a) escarpment, (b) triangular hill, (c) bell-shaped hill. Note, along the abscissa, $1H = \{M_t = 1\}$

two effects leads to high M_t values near the surface where high velocities are being normalised by small velocities. It is for this reason that $M_{t,\max}$ values are considered to give a better picture of true amplification in impinging jet flow. This same shape occurs for all profiles above the crest in Fig. 9. The second type of profile is one that again steadily increases with a decrease in elevation, but this

time rapidly decreases in value just below x/D = 0.02. This behaviour is due to either the flow being within, or affected by, a separation region behind the crest, thus leading to small velocities being normalised by a relatively large velocity. This trend is again present in all lee plots in Fig. 9.

When comparing the numerical predictions in Fig. 9(a) with experimental data excellent agreement is seen for the region below z/H = 3. Above this point the numerical model overestimates the amplification shown through experimentation. There are several reasons why this overestimation is believed to occur. Firstly, due to the axisymmetric nature of the numerical model, it assumes a three dimensional topographic feature that encircles the jet, whereas the experimental model simply uses two dimensional (linear) features. The use of two dimensional features is much more realistic when considering true downburst/topographic interactions, but is unable to be strictly reproduced in an axisymmetric numerical model. This line of reasoning was examined by experimentally testing some three dimensional annular topographic features. It was found that the annular features produced a slightly larger lee vortex which lifted the lee profiles and produced a marginally better fit to the numerical predictions. An example of test results is given for the triangular hill, Φ = 0.2, +2H, Fig. 9(b). Secondly, the velocity values close to the upper elevation limit in are very small, thus even a small difference in measured velocity (due to error or differing upper jet boundary conditions) produces a significant variation in M_t. Using a jet with a higher Reynolds number may help reduce this discrepancy. However, when thinking in design terms, small differences in M_t at these high elevations are somewhat irrelevant as the velocity magnitude is very low, and it is a region where M_t values are below 1.0 (except for lee profiles over steep features), which is a case that would never be prescribed for design.

An example of the full numerical amplification field is given in Fig. 10(a), where a contour plot of M_t values is shown for flow over the steep escarpment. A clear region of high M_t values occur directly above the crest, and a region of low values occur at the base of the rise. This type of behaviour is similar to that for atmospheric boundary layer flow, and is similar to that observed for the shallow escarpment case (not shown). Two unusual regions of high M_t gradients can be observed for elevations $z/H > 3.0$ within the domain shown. The first of these, located directly above the base of the topographic feature, occurs because the separation vortex at ground level lifts the velocity profile vertically, thus misaligning it with the normalising flat surface profile. This process leads to high M_t values for $z/H > 3.0$ as it remains similar in shape and magnitude to the profile over a flat surface. The second region of high M_t gradients occurs directly above the crest. At this position the flow velocity is accelerated close to the local ground surface, leading to a mean velocity profile that peaks at low elevation, then decays with elevation in a similar manner to the case of no topography. This relationship is depicted clearly in Fig. 8 and shows the topographically influenced velocity profiles to be less than the normalising flat surface profiles at large elevations thus leading to the region of low M_t. For the region behind the crest the flow is seen to quickly return to a speed-up factor around 1.0.

For the large, shallow triangular hill, Fig. 9(b), located at x_c = 1.0D and x_c = 1.5D, similar profiles are observed, with Tabl 3 showing similar $M_{t,\max}$ values. However, when looking at the profiles for the small topographic feature it is evident, at least away from the crest, that the profiles have been noticeably displaced vertically. This is because a larger relative separation region, with reference to H, forms behind the small topographic feature. The larger separation region leads to a smaller $M_{t,\max}$ value (compared with flow over the large feature) due to the reduced effective slope. A comparison between the entire acceleration fields for the large and small features is shown in Fig. 10(b) and (c), respectively, which clearly show the differing relative separation regions. Here it is evident that the

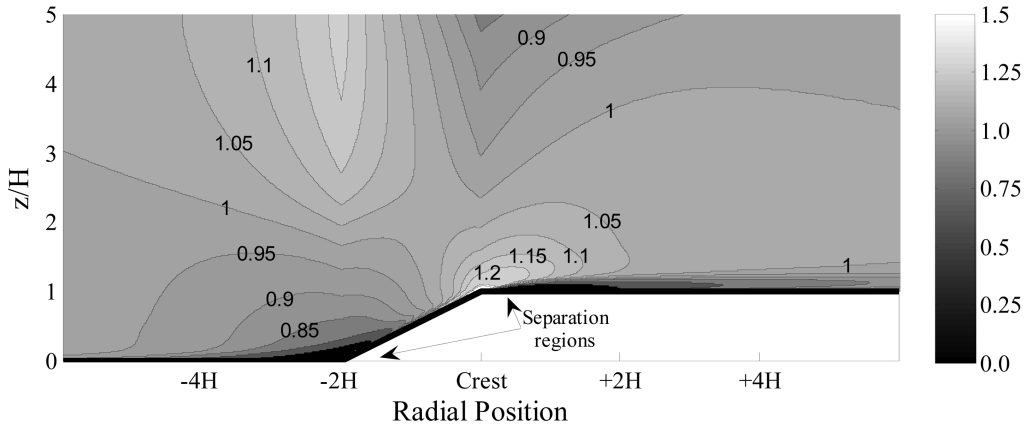

(a) Steep escarpment, $x_c = 1.0D$, $\Phi = 0.5$, $H/D = 0.048$.

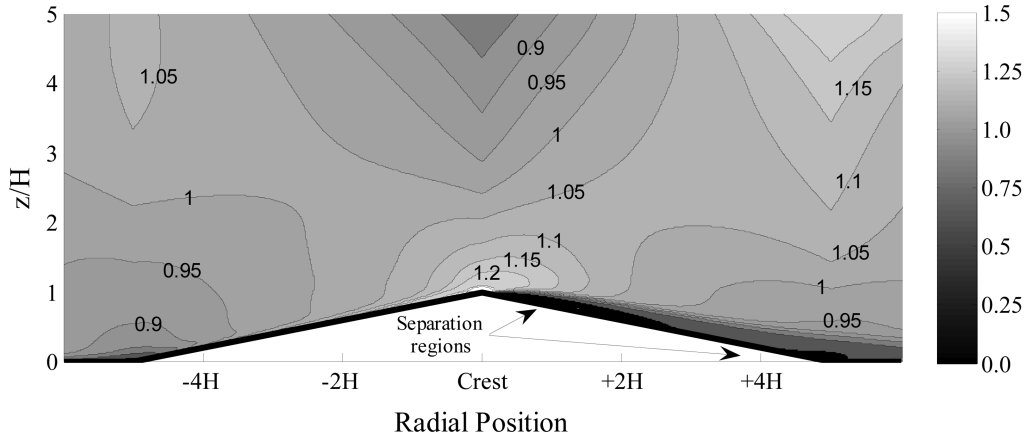

(b) Shallow triangular hill, $x_c = 1.0D$, $\Phi = 0.2$, $H/D = 0.048$.

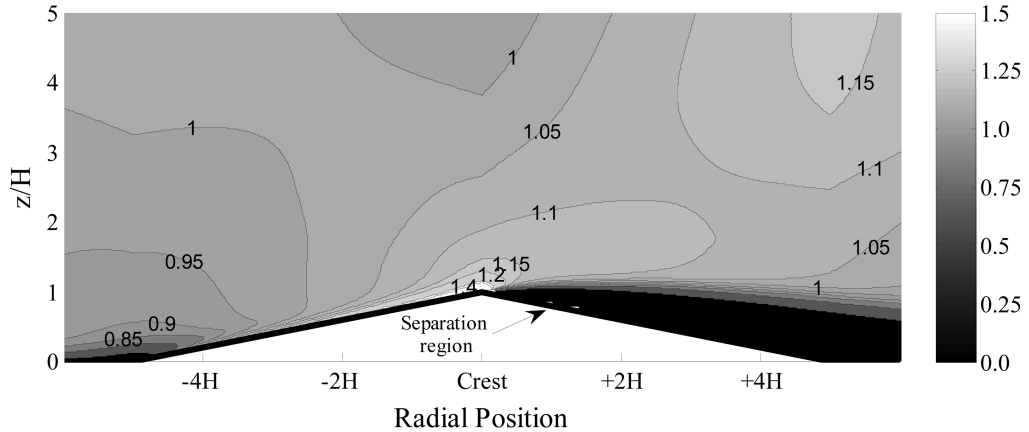

(c) Shallow triangular hill, $x_c = 1.0D$, $\Phi = 0.2$, $H/D = 0.024$.

Fig. 10 Topographic multiplier contour plots for a, (a) steep escarpment, and (b) large, shallow triangular hill, and (c) small, shallow triangular hill. Flow is from left to right

differing values of H have changed the flow from having only a small separation region (based on the size of the topographic feature), to one having a large separation region. This has occurred because the absolute size of the separation region appears to have been maintained between simulations. The replication of absolute separation size was also observed in subsequent experimental simulations with the small (H = 0.024D) topographic feature and numerical simulations with a topographic feature twice the size of the large feature (H = 0.1D). It is not entirely clear why this phenomenon occurs, however, the same behaviour was observed both experimentally and numerically. This suggests it is a real effect but how it scales with Reynolds number and geometric parameters remains to be investigated.

For the steep triangular hill there is again little difference between the profiles above the crest, but for a slight overestimation of amplification at higher elevations by the numerical model. Behind the crest however large differences appear between the three numerical profiles, the difference becoming larger as the radial distance increases. The comparison between experimental and numerical results is reasonable at +1H, but appears to be getting worse as it reaches +2H. For both the profiles at +1H and +2H the small topographic feature produced smaller amplification than the large feature. This is to be expected because the large topographic feature lifts the velocity profile produced behind the crest further up the normalising profile, thus, these velocities are normalised against much smaller velocities (refer Fig. 3). This suggests that when a significant separation region exists the M_t values observed will be dependent on the ratio of H to the wall jet thickness (δ), unlike that observed for the relatively attached flow regimes over the escarpment. Similar reasoning can be used to explain why M_t profiles for x_c = 1.5D are always higher in magnitude than for x_c = 1.0D when looking at the flow above large separation regions. Comparing Fig. 3(b) and (c) it is evident that the decrease in velocity with elevation (i.e., the gradient above the maximum) is greater for x/D = 1.5, which suggests that for a constant displacement of the velocity profile (a constant H suggests that the shear layer will be at approximately the same elevation for both cases) a smaller relative velocity will be used for the normalisation, thus leading to a larger M_t value for the x_c = 1.5D case. In fact, considering $M_{t,\max}$ values at +2H behind the steep crest, results are 1.11, 1.14, and 1.10, for the cases, large feature at x_c = 1.0D, small feature located at x_c = 1.0D, and large feature located at x_c = 1.5D, respectively. These numbers show the actual amplification of maximum velocity is similar in each case, unlike the image portrayed in Fig. 9 for the height specific topographical multiplier.

The flow over the bell-shaped hill has similar amplification results when compared with the triangular hill and due to the similarity in shape the reasoning for similarities and differences are expected to be the same.

It is therefore evident that the numerical model predicts amplification well for the region below about z = 2H above the local surface with a slight overestimation above this point. One reasoning for the overestimation is believed to be because the numerical model assumes a three dimensional hill that surrounds the downdraft while the experimentation simply used a linear two dimensional hill. The experimental results for the two dimensional hills are however expected to be much more realistic when considering actual topography. It was generally found that when flow remained attached to the surface M_t values were independent of both radial position and H/δ ratios. For topographic features where substantial separation occurred however, the opposite was true and M_t values were found to be dependent on both radial position and H/δ ratios. Despite the difference in observed M_t values, little difference was observed for actual amplification of the maximum velocity, $M_{t,\max}$, observed between profiles.

3.3.3. Topographic multiplier comparison to previous work in ABL and simulated downburst flow

A comparison with previous experimental work over escarpments, in simulated downburst and boundary layer flow, is given in Fig. 11. All results in the simulated downburst flow collapse extremely well for z/H < 1 for flow over the shallow escarpment, Fig. 11(a). The three experimental results all represent jets of different cross-sectional shape, profile, and Reynolds number, and represent H/δ ratios ranging from 0.25 (Holmes 1992) to 0.6 (Letchford and Illidge 1999), implying that for elevations up to the height of the topographic feature above the crest the magnitude of amplification in velocity is driven largely by the fact the flow is a non-confined wall jet. This result follows a similar trend to that observed in Fig. 9(a) with the difference between the large and small topographic features in that case being of similar magnitude to the scatter in data shown in Fig. 11(a). For $z/H > 1$ however, results of Letchford and Illidge (1999) diverge significantly from the others. This divergence is expected to be because the velocity profile used by Letchford and Illidge (1999) differs significantly to that used herein, due to the non-circular nature of their jet outlet. In this same region however, the results of Holmes (1992) compare well with the current results despite different Reynolds number (approximately 700,000 compared to 70,000 here) and H/δ values (0.25 compared to 0.35 here); again supporting the hypothesis that the M_t values are relatively independent of H/δ for non-separated flows. Comparing the current simulated downburst topographic multipliers and those obtained in a simulated atmospheric boundary layer, both profiles have a similar shape, but the multipliers for the simulated downburst winds are consistently 15 to 35% lower in magnitude. Comparisons for the shallow triangular and bell-shaped hill show a similar picture with the magnitude of reduction being of the same order. These findings agree with the hypothesis initially put forward by Holmes (1992) that the non-confined nature of the wall jet leads to smaller topographic multipliers than observed for boundary layer flow.

For the steep escarpment case, Fig. 11(b), similar results are observed with a good collapse of data below $z/H = 1$, but a divergence above this level. The results of Letchford and Illidge (1999) and Wood, *et al*. (2001) diverge from the current results for $z/H > 1$. Again, this is expected to be due to differing initial (and therefore normalising) velocity profiles. Comparing the topographic multipliers for the simulated downburst winds to the simulated boundary layer, M_t values due to the simulated downburst winds are of the order of 15 to 35% lower in magnitude again highlighting the large difference in topographic effects for the two types of flow. Similar results were again observed for the triangular and bell-shaped hills.

Letchford and Illidge (1999) suggest that above the crest, the relationship, $M_t = 1 + \Phi$ reasonably approximates the maximum M_t value near the surface with a linear decay to $M_t = 1.0$ at an elevation of $z/\delta = 0.5$. An elevation of $z/\delta = 0.5$ corresponds to $z/H = 0.85$ for Letchford and Illidge (1999), and $z/H = 1.4$ for the present study. This relationship appears to be acceptable for the escarpment features tested, including the numerical predictions in Fig. 9 ($z/\delta = 0.5$ corresponds to $z/H = 2.8$ for the small topographic feature) if the values below $z/H \sim 0.1$ are ignored. However, when considering the hill features, where $\Phi = 0.2$ produces a larger amplification than $\Phi = 0.5$, this relationship is no longer conservative. It is believed that the proposal by Letchford and Illidge (1999) only applies when the slope, Φ, approximates the effective slope seen by the flow, i.e., the flow separation is small. Perhaps instead of Φ, a measure of effective slope may be more useful, though much more difficult to determine.

If however, for codification, a constant velocity is prescribed below the peak for the standard downburst wind, $M_{t,\max}$ could be used as the multiplier in this region while still remaining conservative.

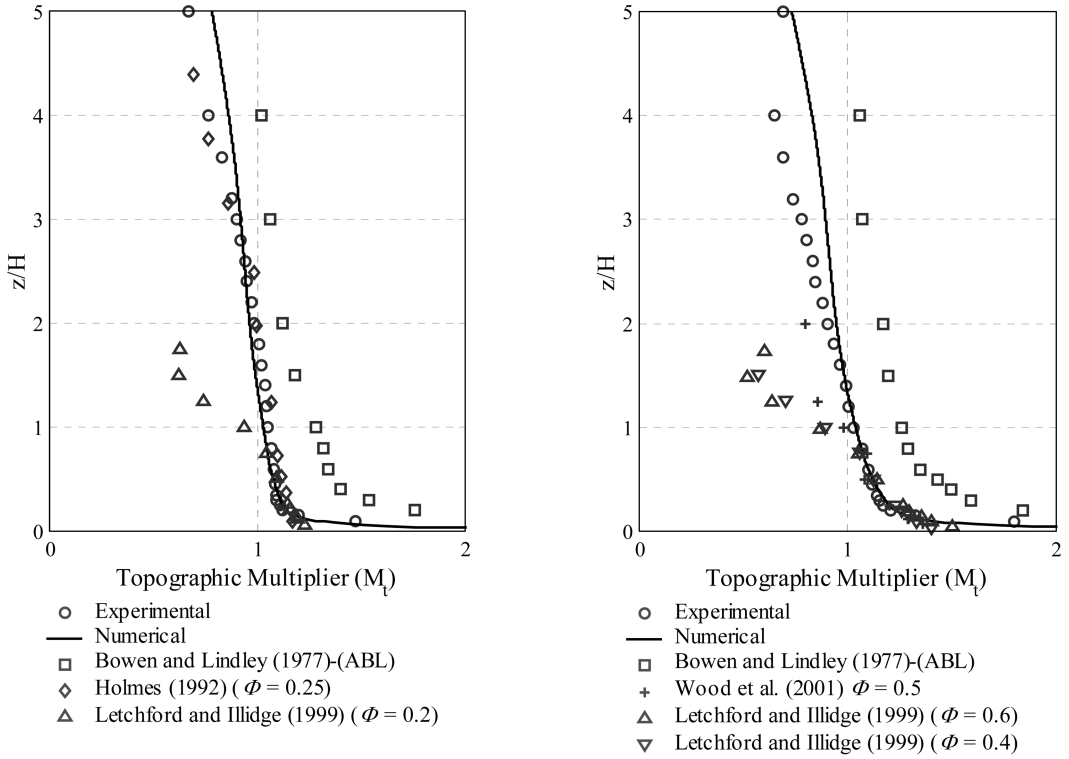

(a) $\Phi = 0.2$. (b) $\Phi = 0.5$.

Fig. 11 Comparison between topographic multipliers for flow over an escarpment measured experimentally by previous researchers in simulated downburst and atmospheric boundary layer flow, and the current numerical and experimental results, (a) $\Phi = 0.2$, and (b) $\Phi = 0.5$

Approximating the region below the peak with a uniform velocity is not unreasonable when viewing the upper bound of JAWS data presented in Fig. 6. Above the peak, a linear decay of velocity speed-up back to 1.0 at z/δ = 0.5 again appears to be an appropriate assumption based on Fig. 9. This approximation to the M_t profile would however only be applicable over the crest of the topography as the lee profiles are based on the displacement of the wall jet due to the separation vortex.

From a codification standpoint, it would be advantageous to use the similarities between the boundary layer and simulated downburst M_t profile shapes. By inspection of Fig. 11, it is evident that a conservative approximation of M_t for the simulated downburst flow can be made by multiplying boundary layer M_t values by a constant. For the escarpment cases of $\Phi = 0.2$ and $\Phi = 0.5$, constant values of 0.9 and 0.85 respectively would apply. A value of 0.9 could be used for all other features tested. This approach would simply utilize M_t values already in standards with the addition of downburst constant.

4. Conclusions

A stationary, long duration thunderstorm downburst has been simulated experimentally and numerically by way of a steady flow impinging air jet. It was found that the Shear Stress Transport (*SST*) turbulence closure scheme was the most successful of the turbulence models available in

ANSYS CFX11 at overcoming the well-known issue of modelling a turbulent impinging jet (Launder and Sandham 2002). Predicted velocity measurements at a series of radial positions were found to compare well with experiments conducted by the authors and measurements by Craft, *et al*. (1993). Both the numerical and experimental velocity profiles were shown to compare well with the upper-bound of the velocity range reported by Hjelmfelt (1988), for the full-scale JAWS microburst monitoring project. This comparison supported the impinging jet model as a simulation technique for a possible type of downburst wind flow.

When considering the flow over topographic features it was found that all features tested amplified the flow velocity above the crest. Of the features tested, the steep escarpment and shallow triangular hill had the largest amplification of maximum velocity ($M_{t,\max}$), with an increase of approximately 25% measured above the crest. It was also found that the topographic features lowered the elevation of maximum velocity. Results presented suggested the numerical model predicted the velocity profiles over topographic features with a good level of accuracy when little or no flow separation occurred (escarpments or shallow hills). It was found however that results diverged from experimental measurements deep in the shear layer formed between the separated wall jet and the re-circulation vortex in the lee of steep hill features. It is believed though that this discrepancy can be somewhat related to the measurement device interfering with the flow being measured.

Converting velocity profiles to topographic multipliers it was found that the numerical model predicted amplification well below about $2H$ above the local surface, but less well above this point, in part, due to differences between the numerical and experimental model (axisymmetric compared with three dimensional respectively). It was generally found that when flow remained attached to the surface M_t values were independent of both the radial position and H/δ ratios, but when substantial separation occurred the M_t values were found to be dependent on both radial position and H/δ ratios. The relative difference in amplification of maximum velocity ($M_{t,\max}$) was however found to be similar for all topographic heights and locations thus suggesting that changes in M_t are simply due to a relative relocation on the normalisation profile.

The conclusion of Holmes (1992) and others that M_t values due to simulated downburst flow were lower than those for boundary layer flow over an escarpment was further confirmed for all topographic features tested. It was found that M_t values for all profiles were up to 35% lower than those measured in boundary layer wind tunnel tests. This information is important when considering design of structures in a mixed wind climate for both low- and high-rise buildings.

A simple code-like approximation for M_t values put forward by Letchford and Illidge (1999) was shown to provide a reasonable conservative approximation for flow over escarpments. However this approximation was shown not to be conservative for hill shape features. Three additional methods of M_t approximation were put forward to address this issue, one based on an effective slope, the second based on $M_{t,\max}$ when using a simplified initial velocity profile, and the third based on the boundary layer M_t profile.

References

ANSYS (2007) *"ANSYS CFX User's Manual"* see www.ansys.com/cfx.

Alahyari, A. and Longmire, E.K. (1995), "Dynamics of experimentally simulated microbursts", *AIAA J.*, **33**(11), 2128-2136.

Anderson, J.R., Orf, L.G. and Straka, J.M. (1992), "A 3-D model system for simulating thunderstorm microburst outflows", *Meteorol. Atmos. Phys.*, **49**(1-4), 123-131.

Bowen, A.J. and Lindley, D. (1977), "A wind tunnel investigation of the wind speed and turbulence characteristics close to the ground over various escarpment shapes", *Boundary-Layer Met.*, **12**(3), 259-271.
Bowen, A.J. (1983), "The prediction of mean wind speeds above simple 2D hill shapes", *J. Wind Eng. Ind. Aerodyn.*, **15**, 259-270.
Chay, M.T. and Letchford, C.W., (2002), "Pressure distributions on a cube in a simulated thunderstorm downburst. Part A: Stationary downburst observations", *J. Wind Eng. Ind. Aerodyn.*, **90**(7), 711-732.
Chay, M.T., Albermani, F. and Wilson, R. (2006), "Numerical and analytical simulation of downburst wind loads", *Eng. Struct*, **28**(2), 240-254.
Choi, E.C.C. (2004), "Field measurement and experimental study of wind speed profile during thunderstorms", *J. Wind Eng. Ind. Aerodyn.*, **92**(3-4), 275-290.
Craft, T.J., Graham, L.J.W. and Launder B.E. (1993), "Impinging jet studies for turbulence model assessment – II. An examination of the performance of four turbulence models", *Int. J. Heat Mass Transfer*, **36**(10), 2685-2697.
Fujita, T.T. (1981), "Tornadoes and downbursts in the context of generalized planetary scales", *J. Atmos. Sci.*, **38**(8), 1511-1534.
Fujita, T.T. (1985), "The downburst: microburst and macroburst", *Satellite and Mesometeorology Research Project (SMRP) Research Paper* 210*, Dept. of Geophysical Sciences, Univ. of Chicago*, 122 pages.
Fujita, T.T. (1986), "DFW Microburst; on August 2, 1985", *Satellite and Mesometeorology Research Project (SMRP) Research Paper* 217*, Dept. of Geophysical Sciences, Univ. of Chicago*, 154 pages.
Fujita, T.T. (1990), "Downburst: meteorological features and wind field characteristics", *J. Wind Eng. Ind. Aerodyn.*, **36**(1-3), 75-86.
Gast, K.D. and Schroeder, J.L. (2003) "Supercell rear-flank downdraft as sampled in the 2002 thunderstorm outflow experiment", *Proceedings of the 11th International Conference on Wind Engineering*, Lubbock, June.
Hangan, H. and Xu, Z. (2005), "Scale and roughness effects in impinging jets with application to downburst simulations", *Proceedings of 2005 Americas Conference on Wind Engineering*, Baton Rouge, May.
Hjelmfelt, M.R. (1988), "Structure and life cycle of microburst outflows observed in Colorado", *J. Applied Meteor.*, **27**(8), 900-927.
Hjelmfelt, M.R., Roberts, R.D., Orville, H.D., Chen, J.P. and Kopp, F.J. (1989), "Observational and numerical study of a microburst line-producing storm", *J. Atmos. Sci.*, **46**(17), 2713-2744.
Holmes, J.D. (1992), "Physical modelling of thunderstorm downdrafts by wind tunnel jet", *Proceedings of the 2nd Australian Wind Engineering Society Workshop on Wind Engineering*, Melbourne, February.
Holmes, J.D. (2003), "A re-analysis of recorded Extreme wind Speeds in region A", *Aust. J. Struct. Eng.*, **4**(1), 29-40.
Holmes, J.D., Baker, C.J., English, E.C. and Choi, E.C.C. (2005), "Wind structure and codification", *Wind Struct.*, **8**(4), 235-250.
Kim, J. and Hangan, H. (2007), "Numerical simulations of impinging jets with application to downbursts", *J. Wind Eng. Ind. Aerodyn.*, **95**(4), 279-298.
Laufer, J. (1954), "The structure of turbulence in fully developed pipe flow", *National Advisory Committee for Aeronautics, Report 1174*, Washington.
Launder, B.E. and Spalding, D.B. (1974), "The numerical computation of turbulent flows", *Comp. Meth. Appl. Mech. Engng.*, **3**, 269-289.
Launder, B.E., Reece G.J. and Rodi W. (1975), "Progress in the development of a Reynolds-stress turbulence closure", *J. Fluid Mech.*, **68**(3), 537-566.
Launder, B.E. (Eds.) and Sandham, N.D. (Eds.) (2002), *Closure strategies for turbulent and transitional flow*, Cambridge University Press, Cambridge, UK.
Letchford, C.W. and Chay, M.T. (2002), "Pressure distributions on a cube in a simulated thunderstorm downburst. Part B: moving downburst observations", *J. Wind Eng. Ind. Aerodyn.*, **90**(7), 733-753.
Letchford, C.W and Illidge, G. (1999), "Turbulence and topographic effects in simulated thunderstorm downdrafts by wind tunnel jet", *Proceedings of the 10th International Conference on Wind Engineering*, Copenhagen, June.
Lin, W.E. and Savory, E. (2006), "Large-scale quasi-steady modelling of a downburst outflow using a slot jet", *Wind Struct.*, **9**(6), 419-440.

Lundgren, T.S., Yao, J. and Mansour, N.N. (1992), "Microburst modelling and scaling", *J. Fluid Mech.*, **239**, 461-488.
Mason, M.S., Letchford, C.W. and James, D.L. (2005), "Pulsed wall jet simulation of a stationary thunderstorm downburst, Part A: Physical structure and flow field characterisation", *J. Wind Eng. Ind. Aerodyn.*, **93**(7), 557-580.
Mason, M.S., Wood, G.S. and Fletcher, D.F. (2007), "A simple atmospheric downburst model for wind engineering application", *Proceedings of the 12th International Conference on Wind Engineering*, Cairns, July, 1447-1454.
Menter, F.R. (1994), "Two-equation eddy-viscosity turbulence models for engineering applications", *AIAA J.*, **32**(8), 1598-1605.
Mousley, P. (2002), *TFI Probe User's Guide*, see www.turbulentflow.com.au.
Orf, L.G., Anderson, J.R. and Straka, J.M. (1996), "A three dimensional numerical analysis of colliding microburst outflow dynamics", *J. Atmos. Sci.*, **53**(17), 2490-2511.
Orf, L.G. and Anderson, J.R. (1999), "A numerical study of traveling microbursts", *J. Atmos. Sci.*, **127**(6), 1244-1258.
Oseguera, R. and Bowles, R. (1988) "A simple, analytical 3-dimensional downburst model based on boundary layer stagnation flow", *NASA TM*, 100632.
Pearse, J.R., Lindley, D. and Stevenson, D.C. (1981), "Wind flow over ridges in simulated atmospheric boundary layers", *Boundary-layer Meteor.*, **21**, 77-92.
Proctor, F.H. (1988), "Numerical simulation of an isolated microburst. Part I: Dynamics and structure", *J. Atmos. Sci.*, **45**(21), 3137-3160.
Proctor, F.H. (1989), "Numerical simulation of an isolated microburst. Part II: Sensitivity experiments", *J. Atmos. Sci.*, **46**(14), 2143-2165.
Selvam, R.P. and Holmes, J.D. (1992), "Numerical simulation of thunderstorm downdrafts", *J. Wind Eng. Ind. Aerodyn.*, **41-44**, 2817-2825.
Standards Australia (1989), *AS 1170.2 – 1989: Minimum design loads on structures. Part 2: Wind loads*, Standards Australia, Sydney.
Standards Australia/Standards New Zealand (2002), *AS/NZS 1170.2:2002: Structural design actions. Part 2: Wind actions*, Standards Australia/Standards New Zealand, Sydney.
Vieser, W., Esch, T. and Menter, F.R. (2004), "Heat transfer predictions using advanced two-equation turbulence models", *CFX-VAL10/0404*.
Vicroy, D.D. (1991), "A simple, analytical, axisymmetric microburst model for downdraft estimation", *NASA-TM-104053*.
Wilcox, D.C. (1986), "Multiscale model for turbulent flows", *In AIAA 24th Aerospace Sciences Meeting*, American Institute of Aeronautics and Astronautics.
Wood, G.S., Kwok, K.C.S., Motteram, N.A. and Fletcher, D.F. (2001), "Physical and numerical modelling of thunderstorm downbursts", *J. Wind Eng. Ind. Aerodyn.*, **89**(6), 535-552.
Yakhot, V., Orszag, S.A., Thangam, S., Gatski, T.B. and Speziale, C.G. (1992) "Development of turbulence models for shear flows by a double expansion technique", *Phys. Fluids A*, **4**(7), 1510-1520.
Yao, J. and Lundgren, T.S. (1996), "Experimental investigation of microbursts", *Exp. in Fluids*, **21**(1), 17-25.
Yap, C.R. (1987), "Turbulent heat and momentum transfer in recirculating and impinging flows", Ph.D. thesis, Faculty of Technology, University of Manchester.

JH